

## Full length article

# Enhancing strength and strain hardenability via deformation twinning in fcc-based high entropy alloys reinforced with intermetallic compounds



Deep Choudhuri <sup>a, b,\*</sup>, Bharat Gwalani <sup>a, b</sup>, Stephane Gorsse <sup>c, d</sup>,  
Mageshwari Komarasamy <sup>b</sup>, Srinivas A. Mantri <sup>b</sup>, Srivilliputhur G. Srinivasan <sup>b</sup>,  
Rajiv S. Mishra <sup>a, b</sup>, Rajarshi Banerjee <sup>a, b, \*\*</sup>

<sup>a</sup> Advanced Materials and Manufacturing Processes Institute, University of North Texas, Denton, TX, 76207, USA

<sup>b</sup> Department of Materials Science and Engineering, University of North Texas, Denton, TX, 76207, USA

<sup>c</sup> CNRS, ICMCB, UMR 5026, 33600, Pessac, France

<sup>d</sup> Bordeaux INP, ENSCBP, 33600, Pessac, France

## ARTICLE INFO

## Article history:

Received 1 June 2018

Received in revised form

8 November 2018

Accepted 7 December 2018

Available online 10 December 2018

## ABSTRACT

Twinning is a key deformation mechanism in face-centered-cubic (fcc)-based and some body-centered-cubic (bcc)-based alloys, which imparts excellent strength-ductility combination by increasing strain-hardenability. Typically, twinning in fcc-based alloys increases when the stacking fault energy is lowered via changes in composition. The present study clearly demonstrates that deformation twinning can be enhanced when hard-intermetallic compounds like ordered B2 and sigma phases form in the fcc matrix of a high entropy alloy (HEA), leading to an excellent combination of strength, ductility, and strain-hardenability. Such a combination of properties was achieved by exploiting the novel and often unusual phase stability regimes that can be accessed in these complex concentrated HEAs. The present study exploits a unique three-phase mixture of recrystallized fine-grained fcc + B2 + sigma in a prototypical Al<sub>0.3</sub>CoCrFeNi HEA to demonstrate this effect. Coupling transmission electron microscopy and molecular dynamics simulations revealed that B2 grains enhance deformation twinning by raising the local stress levels, consequently forming substantially thicker twins as compared to the single fcc-phase condition of Al<sub>0.3</sub>CoCrFeNi. The local stresses were further accommodated via nano-twinning, limited B2 plasticity, and highly restricted micro-cracks in and around the sigma grains.

© 2018 Acta Materialia Inc. Published by Elsevier Ltd. All rights reserved.

## 1. Introduction

Many metallic alloys undergo strain- or work hardening during plastic deformation, during which the flow stress or strength of the material continually varies with plastic strain [1,2]. Low stacking fault energy face-centered-cubic (fcc) alloys are particularly susceptible to {111} <112> deformation twinning. In this process, the lattice reorients to form mirror images across a (111) plane or  $\Sigma_3$  boundary [3], which substantially improves strain hardenability of

such materials [4–7]. Twins increase flow stress by blocking mobile dislocations, and, depending on twin volume fraction in the deformed state, contribute to the plastic strain via twinning shear of  $\frac{1}{\sqrt{2}}$  [1,3,7]. Consequently, deformation twinning, in high volume fraction, is uniquely suited to exceptionally enhance strength, ductility and toughness in fcc-based alloys. The recently developed fcc-based TWIP (twinning induced plasticity) steels are attractive for damage tolerant applications [1,4–6].

In recent years, a relatively new category of materials called high-entropy alloys (HEAs) or complex concentrated alloys (CCAs) with fcc-base have exhibited a promising combination of strength, ductility and toughness [8,9]. HEAs/CCAs are typically solid solutions without any “dominant” element, but with typically four to five constituent elements that appear in equiatomic concentrations. Notable examples include CoCrFeNi, CoCrFeNiMn,

\* Corresponding author. Advanced Materials and Manufacturing Processes Institute, University of North Texas, Denton, TX, 76207, USA.

\*\* Corresponding author. Advanced Materials and Manufacturing Processes Institute, University of North Texas, Denton, TX, 76207, USA.

E-mail addresses: [deep.choudhuri@unt.edu](mailto:deep.choudhuri@unt.edu), [deep.choudhuri@gmail.com](mailto:deep.choudhuri@gmail.com) (D. Choudhuri), [Raj.Banerjee@unt.edu](mailto:Raj.Banerjee@unt.edu) (R. Banerjee).

CoCrFeNiCu, or with minor solute additions to an equiatomic base such as  $\text{Al}_x\text{CoCrFeNi}$  ( $x = 0\text{--}0.3$ ) or  $\text{Al}_x\text{CoCrFeNiCu}$  ( $x = 0\text{--}0.3$ ) [8–10]. Most of these fcc-based HEAs have very low stacking fault energies ( $6\text{--}30 \text{ mJ/m}^2$  [8,11,12]) and form twins during deformation [13–16]. CoCrFeNiMn, another prominent HEA [8,9], is known to deform via nanoscale twinning at the onset of fracture and undergoes ductile failure [13]. Interestingly, it exhibits extensive twinning at cryogenic temperatures (77K) but minimal twinning at room temperature and above [14]. Other HEAs like  $\text{Al}_{0.1}\text{CoCrFeNi}$  also form only a small volume fraction of nanoscale twins under quasistatic tension at room temperature [15,16]. However, severe plastic deformation induced via cold rolling, high strain rate deformation, or high-pressure torsion is known to cause extensive twinning in fcc-based HEAs [17–19], presumably triggered by the higher internal stresses created during deformation [20–23]. Here, we engineer HEA with local microscopic stress raisers to enhance deformation twinning, which hypothesized will lead to an excellent combination of strength and ductility or strain-hardenability. We have achieved such an engineered microstructure, without changing the alloy composition, by exploiting the relative phase stabilities of a well-known fcc-based HEA.

Our work was motivated by a recent discovery that microstructure of a well-known fcc-based  $\text{Al}_{0.3}\text{CoCrFeNi}$  HEA can be dramatically transformed to a duplex fcc-bcc ordered B2 by tuning the cold rolling percentage and then annealing at a temperature of  $800^\circ\text{C}$  [19]. In principle, the B2 grains in this duplex structure can act as Eshelby type inclusion [24] and raise local stress levels during deformation to trigger twinning [25]. In this work, we have also incorporated an additional sigma phase by nominally maintaining the same level of cold rolling [19], but annealing at a lower temperature of  $620^\circ\text{C}$  which stabilizes both B2 and sigma phases [26]. The harder sigma phase is expected to further increase the local stress levels compared to the duplex fcc-B2 microstructure. The resulting fcc-B2-sigma triplex microstructure deformed via a *hierarchy of mechanisms* selected by the local microstructure. For example, near fcc-B2 multiphase grain clusters an order of magnitude larger deformation twinning was observed than in a single-phase fcc microstructure. By coupling TEM and molecular dynamics simulations, we found that twinning was partly enhanced by Kurdjumov-Sachs orientation relationship shared between fcc-B2 grains which served to increase local stress levels during deformation. On the other hand, local stresses near fcc-B2-sigma multiphase grain clusters were accommodated via surprisingly constrained cracking of sigma grains, dislocation plasticity in fcc and B2, and nano-scale twinning within fcc. Together, these mechanisms resulted in excellent strain-hardenability and a good combination of strength (yield strength  $\sim 850 \text{ MPa}$  and ultimate tensile strength  $\sim 1 \text{ GPa}$ ) and ductility ( $\sim 30\%$ ), which are comparable to TWIP steels and better than many commercial titanium alloys. More importantly we have demonstrated in a known HEA that one can improve the twinnability and strain hardenability via in-situ formation of hard grains of an intermetallic compound.

## 2. Experimental and computational methods

### 2.1. Alloy and heat treatments conditions

Complex concentrated alloy of composition 6.7%Al-23.1%Cr-23.4%Cr-23.4%Fe-23.4%Ni (at.%) or  $\text{Al}_{0.3}\text{CoCrFeNi}$  was arc-melted in a vacuum furnace. The cigar-shaped as-cast specimens were then solutionized at  $1150^\circ\text{C}$  for 1H (Fig. 1a) and was subsequently cold rolled to  $\sim 90\%$  thickness reduction (Fig. 1b). The cold rolled strips were further subjected to two different annealing heat treatments to at  $620^\circ\text{C}$  for 50H (Fig. 1c), and  $1150^\circ\text{C}$  for 30 min (Supplementary Fig. 1d). Supplementary Fig. 1 depict the entire

thermomechanical process adopted to produce two distinct refined and coarse microstructures. The selection of the final annealing temperatures was guided by our past thermodynamic calculations using ThermoCalc's TCHEA2.0 database [26].

### 2.2. Mechanical and microstructural characterization

Representative mini tensile dog bones of gauge length  $\sim 5 \text{ mm}$ , width  $\sim 1 \text{ mm}$  and thickness  $\sim 0.3 \text{ mm}$  were extracted from both microstructures using an electric discharge machine. The rectangular cross-section tensile specimens were deformed under uniaxial tension at a strain rate of  $\sim 10^{-3} \text{ s}^{-1}$  in room temperature using a mini-tensile tester [27,28]. Based on testing of three specimens in each condition, the standard deviation is  $\pm 55 \text{ MPa}$ . For each condition, at least three to four tests were conducted. Microstructural characterization of pre- and failed conditions was carried out using a FEI NovaNano scanning electron microscope (SEM) outfitted with a Hikari Super<sup>TM</sup> electron backscattered diffraction (EBSD) system, and FEI Tecnai F20-FEG<sup>TM</sup> transmission electron microscope operating at  $200 \text{ kV}$ . TEM foils were prepared via focused ion beam (FIB) milling in a FEI Nova NanoLab 200<sup>TM</sup>. To ensure that TEM examination of deformation features is performed for nominally uniaxial stress condition, FIB-based TEM foils were plucked from the gauge section, which was at least  $\sim 2\text{--}3 \text{ mm}$  away from the failed neck in the mini-tensile specimens. Furthermore, in certain cases TEM was also used to measure local nano-scale composition, i.e. via energy dispersive spectroscopy (EDS), using EDAX model Tecnai 20T/20ST and Si detector.

### 2.3. Molecular dynamics (MD) simulations

Calculations were carried out using the well-known Large-scale Atomic/Molecular Massively Parallel Simulator (LAMMPS) code [29]. These simulations track the local structure and deformation mechanisms in our prototypical systems as a function of simulation time and strain over nanometer length scales and picosecond time scales. Atomic interactions were described using the Ni-Al-Co embedded atom method (EAM) potential of Purja, Yamakov, and Mishin [30]. This potential accurately described the interatomic spacing, elastic constants, stacking fault energies, and relative stabilities of Ni and NiAl–B2 well. The  $50 \times 20 \times 10 \text{ nm}^3$  simulation boxes used in this work comprised of six grains (one B2 and five fcc) with a total of 909362 atoms (33846 Al and 875516 Ni atoms). This 3D multicrystal ensemble was created using Voronoi tessellation [31,32]. All simulations were carried out with periodic boundary conditions across the three orthogonal directions. Prior to applying deformation, the systems were relaxed using the conjugate gradient method implemented in LAMMPS using energy and force tolerances of  $10^{-6} \text{ eV}$  and  $10^{-6} \text{ eV}/\text{\AA}$ . The so minimized were then deformed under uniaxial tension at strain rates of  $10^7$  and  $10^9 \text{ 1/s}$ . Deformation was carried out at  $300\text{K}$  using Nöse-Hoover method to minimize stresses in the directions transverse to the applied tension. Note that the small times scales accessible to typical MD simulations restricted us to the high strain rates employed here [34,35]. We have also compared all the fcc-B2 microstructures with control fcc-Ni multicrystal ensembles to deduce the influence of the harder B2 phase on the deformation of the surrounding fcc Ni grains. Simulations were analyzed using the OVITO software [36], which allowed us to using common neighbor analysis (CNA) to distinguish between fcc (green color), B2 (blue color), and stacking faults (red) atoms. The atoms near interfacial region and other crystalline defects did not correspond to these known structures and was colored white. The Dislocation analysis (DXA) algorithm implemented in OVITO was used to characterize dislocations in our simulations [36,37].

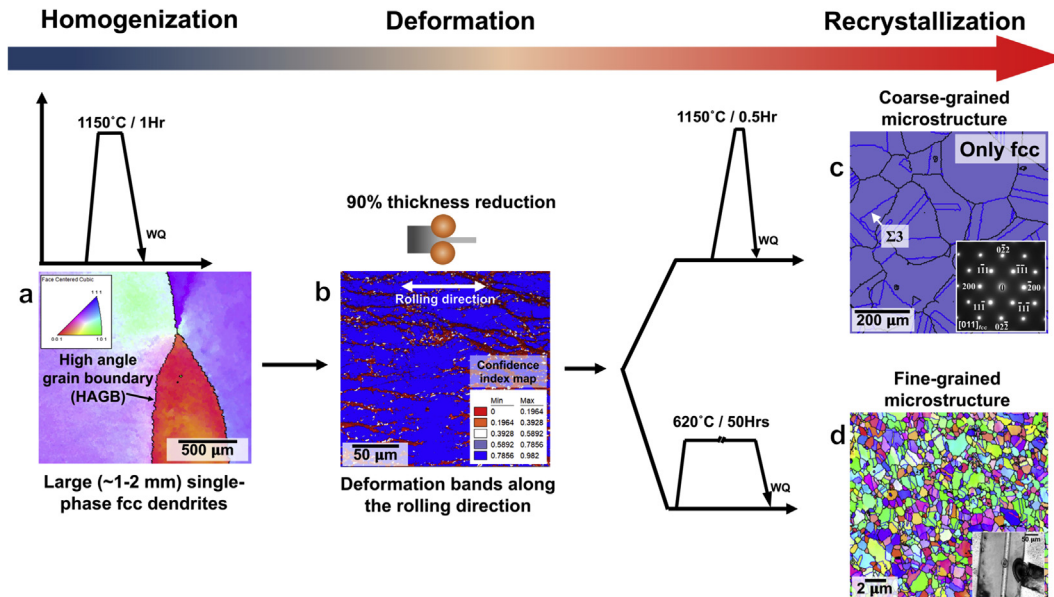


**Fig. 1.** EBSD characterization of microstructures obtained at different stages of thermomechanical processing used in this study. Insets in (c) and (d) show the [011] diffraction pattern and annealing twins in the fcc grains, respectively.

### 3. Results

#### 3.1. Processing conditions and initial microstructures

A combination of conventional cold-rolling and subsequent isothermal annealing was adopted to generate two distinct microstructures from the same Al<sub>0.3</sub>CoCrFeNi HEA. Microstructures at different processing step was characterized with EBSD (see Fig. 1). The homogenized microstructure, comprising of large fcc phase dendrites (1–2 mm in Fig. 1a), was first cold rolled to 90% thickness reduction. Detailed characterization of the cold rolled microstructure is given elsewhere [26]. Here we present the heavily deformed microstructure using a confidence index map, which showed deformation bands along the rolling direction (Fig. 1b). The cold rolled specimens were subsequently annealed at a higher (1150 °C for 0.5H) and lower (620 °C for 50H) temperatures to produce coarse equiaxed grains (~100 µm, Fig. 1b) and refined (1–3 µm, Fig. 1a) microstructures. Note that annealing twins, of differing thicknesses, were noted in case of both types of microstructures, and they are shown with  $\Sigma 3$  boundaries in Fig. 1c for the coarse-grained microstructure and as an inset bright-field TEM (BFTEM) image in Fig. 1d. The coarse-grained microstructure comprised of single-phase fcc grains, which is also corroborated with a representative [011] selected area diffraction pattern (SADP) that contained only the primary fcc reflections without any discernable extra-precipitate reflections. Our past work on Al<sub>0.3</sub>CoCrFeNi HEA [19,26] has showed that only fcc phase is stable at 1150 °C, while secondary intermetallic phases form at/below 1000 °C for this composition. Therefore, the refined microstructure obtained upon annealing at 620 °C for 50H (620 °C/50H), shown in Fig. 1d, contains additional phases, and their crystallography and distribution were investigated in detail using TEM and EBSD.

The complexity of the 620 °C/50H microstructure is depicted in Fig. 2a–g. The bright-field TEM image shown in Fig. 2a shows a B2 grain sandwiched between two fcc grains. The B2 phase is confirmed by the (001)<sub>B2</sub> superlattice reflections seen in the [011] B2 zone axis microdiffraction pattern (Fig. 2b). This TEM image was recorded by orienting the fcc grain close to its [111] zone axis (Fig. 2c), which aligned the B2 grain along [011] in parallel;

indicating that the B2 and fcc grains share an orientation relationship (OR). Their mutual OR was also examined using EBSD that provided a statistical sampling, and Supplementary Fig. 1 shows a representative dataset where a B2 grain is surrounded by four fcc grains, and their respective (011) and (111) pole figures. We find that the B2 grain shares a Kurdjumov-Sachs (KS) OR, i.e. (011)<sub>B2</sub>//(111)<sub>fcc</sub> and [111]<sub>B2</sub>//[011]<sub>fcc</sub>, with only one fcc grain (Supplementary Fig. 1). Annealing at 620 °C also formed sigma ( $\sigma$ ) phase, which is shown with a darker diffracting contrast in the BFTEM shown in Fig. 2d. Microdiffraction patterns recorded along [100] $\sigma$  and [110] $\sigma$ , in Fig. 2e and f respectively, establishes the crystal structure to be  $\sigma$ , with space group P<sub>4</sub> 2/mnm. Thus, the 620 °C/50H heat treatment produced a three-phase microstructure containing grains of fcc, ordered B2 and  $\sigma$  – hereon referred as the “triplex microstructure”. The relative phase distribution in the triplex microstructure is shown via the EBSD phase map in Fig. 2g, which revealed that the relative phase fractions of fcc, B2 and  $\sigma$  were ~80, 10 and 10%, respectively. The EBSD phase map also shows KS-related interfaces are marked in bold red, and that each B2 grain maintains the KS OR with atleast one neighboring fcc grain (also see Supplementary Fig. 1). This 2D representation further allowed us to roughly categorize the triplex microstructure into two distinct multiphase grain-clusters at the micron-scale: (i) binary fcc-B2 and (ii) ternary fcc, B2 and  $\sigma$ . Regions with both types of multiphase grain clusters are marked with dotted rectangles, i.e. I and II, in Fig. 2g, and their respective effects on the deformation mechanisms will be discussed in latter sections.

While the B2 grains are primarily located at fcc grain boundaries (Region I in Fig. 2g), a very low volume fraction (~0.02%) of ellipsoidal-shaped B2 precipitates were also found within the fcc grains. These intragranular B2 precipitates are shown via dark-field TEM (DFTEM) and BFTEM images in Fig. 3a and b, respectively. Fig. 3c shows the STEM-EDS analysis of a fcc-B2 region, which revealed that the B2 phase composition was 18.4Al-14.0Co-2.1Cr-11.0Fe-54.6Ni (at.%), while the fcc matrix composition was 1.5Al-27.1Co-22.8Cr-27.4Fe-21.2Ni (at.%). Note the Al enrichment in the B2 (and the corresponding Al depletion in fcc) resulted in a fcc matrix composition comparable to Al<sub>0.1</sub>CoCrFeNi HEA (Fig. 3c). Qualitative and quantitative STEM-EDS analysis (Fig. 4a and b,

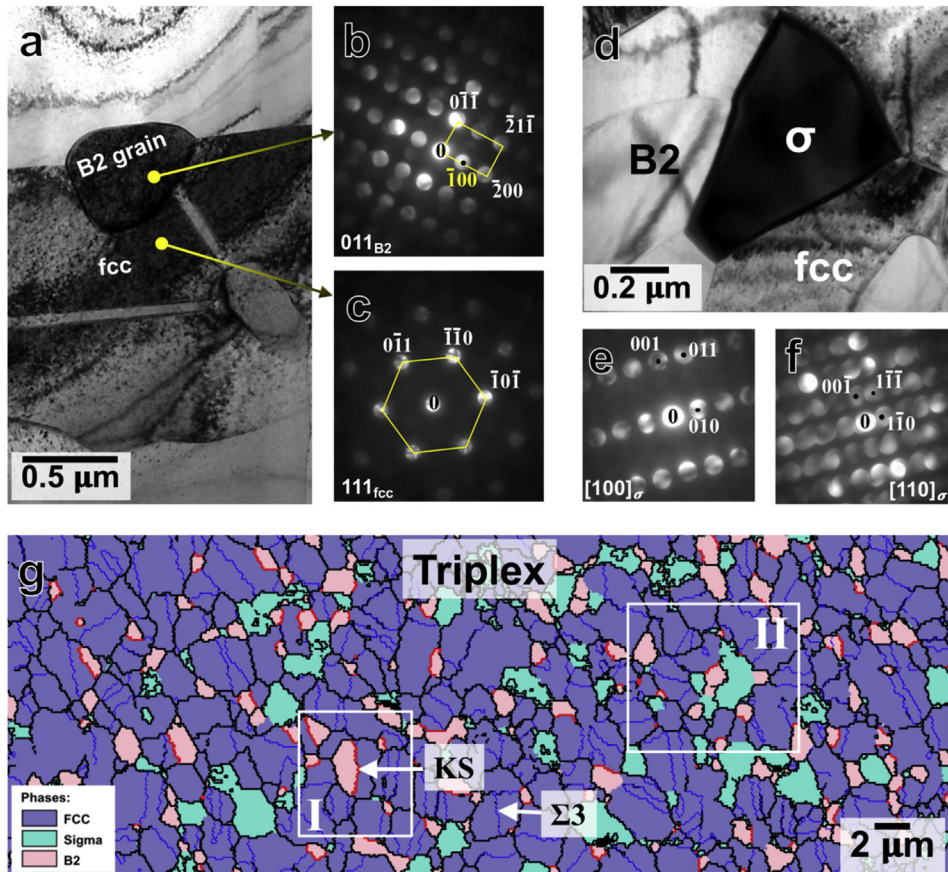


**Fig. 2.** TEM results showing different phases in the triplex microstructure: (a) bright-field TEM (BFTEM) image of intermetallic B2 and fcc grains, while (b)  $[011]_{\text{B}2}$  and (c)  $[111]_{\text{fcc}}$  are microdiffraction patterns from the B2 and a neighboring fcc grains in that BFTEM. (d) BFTEM of sigma ( $\sigma$ ) phase in darker contrast, and the corresponding micro-diffraction patterns recorded at (e)  $[100]_{\sigma}$  and (f)  $[110]_{\sigma}$  zone axes. (g) EBSD phase-map showing the distribution of fcc, B2 and  $\sigma$  phases in the triplex microstructure, along with multiphase grain clusters of fcc-B2 (region I) and fcc-B2- $\sigma$  (regions II). In the solid red lines in the phase-map indicate the interfaces between fcc and B2 grains that are related via Kurdjumov-Sachs (KS) orientation relationship between fcc and B2 grains in (a). (For interpretation of the references to color in this figure legend, the reader is referred to the Web version of this article.)

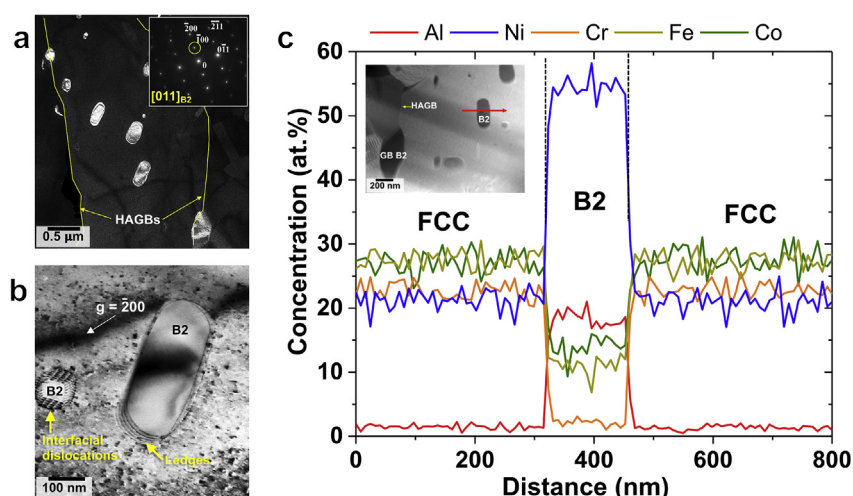


**Fig. 3.** TEM of intragranular B2 precipitates within fcc grains of our triplex microstructure. (a) Dark-field TEM image showing the distribution of B2 precipitates within fcc grain. (b) Bright-field TEM image showing misfit dislocations ledges at fcc-B2 precipitate interfaces. (c) Quantitative STEM-EDS line profile show the partitioning of Al, Co, Cr, Fe and Ni concentrations across the B2 precipitates and their parent fcc grains. Inset of (c) shows the location where the STEM-EDS was performed. The fcc matrix appears to acquire  $\text{Al}_{0.1}\text{CoCrFeNi}$  composition after B2 formation.

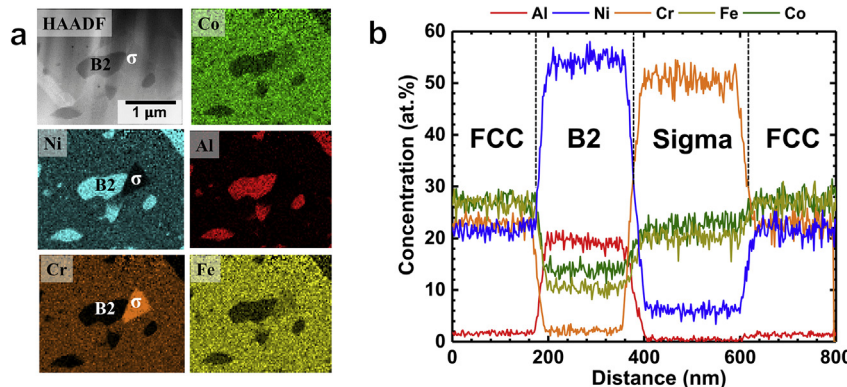


**Fig. 4.** (a) Qualitative STEM-EDS showing elemental distribution near fcc-B2- $\sigma$  (sigma) grain clusters. (b) STEM-EDS line profile quantifies the elemental content in fcc, B2 and  $\sigma$ .

respectively) was also performed in Region-II (in Fig. 2g) that comprised of ternary fcc, B2 and  $\sigma$  phases. Results indicated that the  $\sigma$  phase is rich in Cr, with composition 0.5Al-22.6Co-50.7Cr-20.3Fe-6.0Ni (at.%), while the composition of fcc and B2 phase did not show significant changes compared to Region-I. In other words, the STEM-EDS results indicated that the 620 °C/50H microstructure may have reached uniform compositional distribution among the three constituent phases.

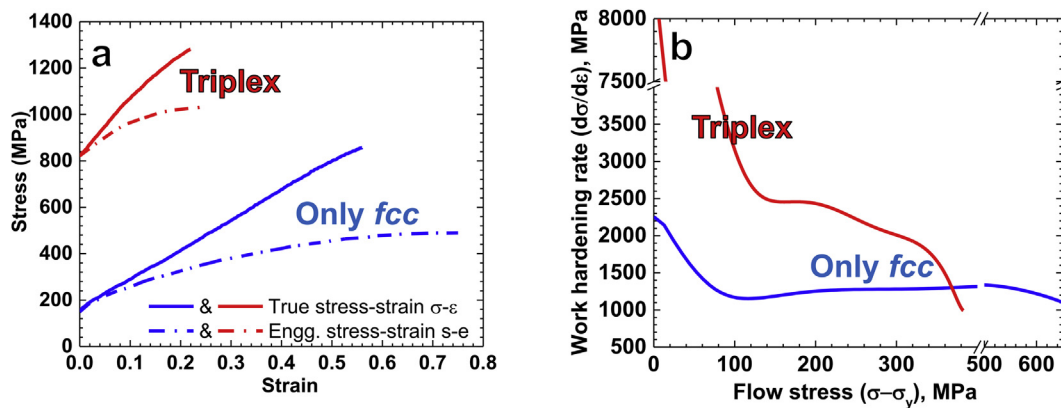
### 3.2. Mechanical responses

The refined triplex microstructure had a much higher strength (avg. YS ~840 MPa and UTS ~1050 MPa) compared to the coarse-grained single-phase fcc microstructures (see Fig. 5a and Table 1), as expected, and exhibited good tensile ductility (avg. elongation strain to failure ~30%). Such good combination of high strength and reasonable ductility in the triplex microstructure was somewhat surprising because brittle intermetallic compounds (e.g.  $\sigma$  and B2 phases) covered large area fraction (~20%) of the triplex microstructure (Fig. 2g), and such brittle intermetallic compounds are expected to reduce ductility. The effect of B2 and  $\sigma$  phases on the deformation behavior of this HEA will first be analyzed by comparing the stage-III work-hardening plots of the triplex and single phase HEA microstructures (Fig. 5b). A close examination of the plot for single phase showed the presence of subtle inflection points or “kinks”, and these kinks seem to be manifest more prominently in the triplex microstructure along with a substantially higher work-hardening rate. Literature suggest that such

kinks are often associated with twinning in low stacking fault materials [21,39,40]; much like those seen in the present study. Notwithstanding, the work-hardening plot suggest that deformation mechanisms prevalent in these fcc-HEAs may have been altered/amplified by the intermetallic compounds. Therefore, the details of the deformation features in the single-phase fcc and triplex three-phase microstructures, subsequent to tensile testing to failure, have been characterized using TEM, and have been described in the following sections.

### 3.3. Deformation of the single fcc-phase microstructure

The intergranular regions within the coarse-grained (~100 μm) single-phase fcc specimens predominantly consisted of deformation bands. Fig. 6a shows that their edges lie along  $(\bar{1}\bar{1}1)$  slip traces which indicated that these bands are caused by  $\{111\}<110>$  planar slip [14,16] and these deformation bands contain a high density of dislocations. Additionally, a closer examination of the regions inside these bands revealed the presence of nano-scale “linear features” that are parallel to the  $(\bar{1}\bar{1}1)$  plane (indicated with arrows in Fig. 6b). These fine-scale features had a very low volume fraction since they did not manifest as extra reflections in the [011] SADP (inset of Fig. 6a), neither were their size-scales permissible for microdiffraction. Therefore, high resolution phase-contrast TEM imaging was used, shown in Fig. 6c, which revealed them as very fine scale (~1 nm thick) twins bounded by  $1/6<112>$  Shockley partials. Since these observations were carried near the center of the coarse grains, our results indicate that twinning was initiated

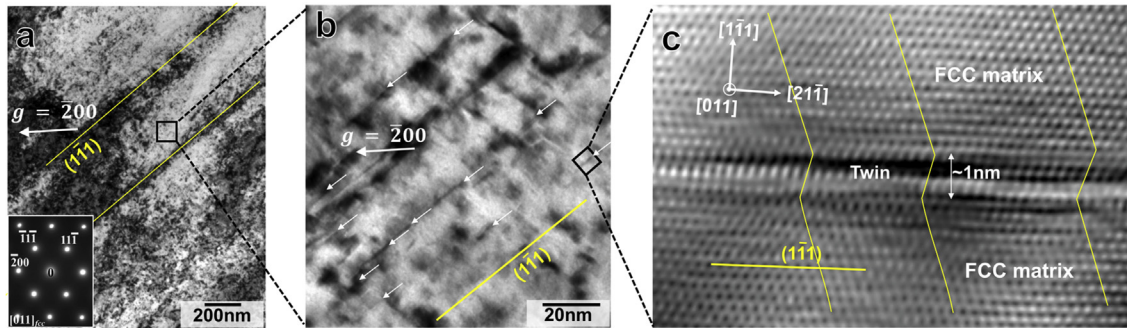


**Fig. 5.** Comparison of mechanical responses of the triplex and single-phase microstructures: (a) true and engineering stress-strain plots, and the corresponding (b) work hardening plots.

**Table 1**

Summary of mechanical properties.

Materials	Yield Strength (MPa)	Ultimate Tensile Strength (MPa)	Ductility (%)
Single-phase fcc (this study)	159 ± 22	410 ± 42	65 ± 3 <sup>a</sup>
Fcc-B2- $\sigma$ Triplex (this study)	840 ± 20	1039 ± 21	32 ± 4 <sup>a</sup>
Al <sub>0.1</sub> CoCrFeNi ([38])	160 ± 7	389 ± 42	44 ± 14 <sup>b</sup>

<sup>a</sup> Elongation until failure.<sup>b</sup> Uniform elongation till the onset of necking.

**Fig. 6.** TEM results showing different deformation features in the single-phase microstructure. (a) and (b) are BFTEMs recorded with  $g = \bar{2}00$  at lower and higher magnifications respectively. (a) A lower magnification BFTEM image showing deformation band aligned with (111) slip trace, which indicates  $\frac{1}{2}<110>$  planar slip. (b) A higher magnification BFTEM image of fine-scale features, marked by arrows, inside the deformation band shown in (a). (c) High resolution phase-contrast image of one of the fine scale features in (b) reveals ~1 nm thick nano-scale twins. The twins appear to have a low volume fraction because they did not manifest as extra reflection in the [011]<sub>fcc</sub> SADP that was recorded with a large area aperture (see the inset of (a)). The TEM of single-phase microstructure indicate that involves a combination of extensive dislocation plasticity and nano-twinning.

via interaction between partials – consistent with previous reports in the literature [20,22]. Thus, TEM observation of the deformed condition indicates that {111} slip band formation and nano-twinning within such bands are the dominant deformation mechanisms in case of the single-phase specimens.

#### 3.4. Deformation of the three-phase triplex microstructure

Distinct differences were observed between the deformation behavior of the single fcc-phase microstructure and the fcc matrix in case of the triplex microstructure. These differences were specifically noted in the vicinity of the fcc-B2 (Fig. 7) and fcc-B2- $\sigma$  (Fig. 8) multiphase grain clusters (as defined in Fig. 1i). We first focused on the fcc matrix near the fcc-B2 grain clusters (Fig. 7a–c), which exhibited coarser deformation twinning. In Fig. 7a the twins distinguished from the parent matrix by recording micro-diffraction patterns from the [011] zone axis, where Fig. 7b and b represent [011] patterns were obtained from the twinned and matrix, respectively. We find that, unlike the extremely thin deformation twins observed within the fcc matrix in case of the single-phase microstructure, the deformation twins in case of the triplex microstructure were an order of magnitude coarser (~15 nm thick). This observation is rather counterintuitive since deformation twinning is typically thought to be inhibited in a fine-grained microstructure [21], and the fcc grain size in the triplex microstructure is ~1–5  $\mu\text{m}$  (see Fig. 2g). Furthermore, the coarser deformation twins were also slightly “bent” at certain locations (marked with arrows in Fig. 7a), which indicated that they may have interacted with intersecting dislocations. Twin-twin interaction between two variants is also shown in Fig. 7d. A careful examination of that region indicated that two parallel twins emanated in the vicinity of the fcc-B2 triple junction (marked as variant “2” in Fig. 7d), while another variant “1”, lying on a conjugate (111) plane, appeared to have originated from the HAGB. Regions exhibiting a patchy dark contrast throughout the image shown in Fig. 7d, correspond to dense dislocation forests. Within these patchy

regions, fine-scale twins and stacking faults (SFs) were also noted; especially near the ellipsoidal intragranular B2 precipitates (Fig. 7e and f). Furthermore, it may be emphasized that the composition of the fcc grains in the triplex microstructure is close to Al<sub>0.1</sub>CoCrFeNi (Figs. 3 and 4), and our recent work on coarse and fine grained fcc-based Al<sub>0.1</sub>CoCrFeNi HEA indicated that such an alloy contains via nano-scale twins in the deformed condition [16]; comparable to single-phase Al<sub>0.3</sub>CoCrFeNi seen in Fig. 6. Therefore, it can be concluded that formation of coarse deformation twins in the fcc matrix in the fcc-B2 grain clusters of the triplex microstructure, was directly influenced by the B2 grains, i.e. Region-I (Fig. 2g).

On the other hand, coarse deformation twins were absent in the fcc matrix in the fcc-B2- $\sigma$  multiphase clusters in Region-II of Fig. 2g; instead deformation features of these regions could be characterized by a complex mixture of micro-mechanisms, which are shown with a BFTEM in Fig. 8a that was recorded from the triple junction of three phases. Inside the fcc grains the individual dislocation segments and dislocation-dislocation interactions are clearly visible, and, in most cases, the dislocation segments appear to be “bowing out” due their interaction with nanoscale twins which are seen as very fine linear features in Fig. 8b (marked with arrows). In other words, these nanoscale twins are acting as impediments to dislocation motion, which, in turn, is expected to increase the overall strain-hardenability of the triplex microstructure. Unlike the single-phase microstructure (Fig. 6), where the nature of the deformation twinning was largely uniform and comprised of only few nanometers thick twins, the fcc-B2- $\sigma$  triplex microstructure, exhibits deformation twins spread over a wider range of thicknesses, differing by atleast an order of magnitude from few nanometers to tens of nanometers.

Additionally, deformation within the two harder intermetallic phases, i.e. B2 and  $\sigma$ , has also been investigated. B2 deformation was first examined by probing the fcc-B2 interfacial regions (marked in Fig. 8c) using  $\mathbf{g}-\mathbf{3g}$  weak beam dark field (WBDF) technique. Fig. 8c and d shows dislocation arrangement within B2 grain and features resembling stacking fault contrast that extend

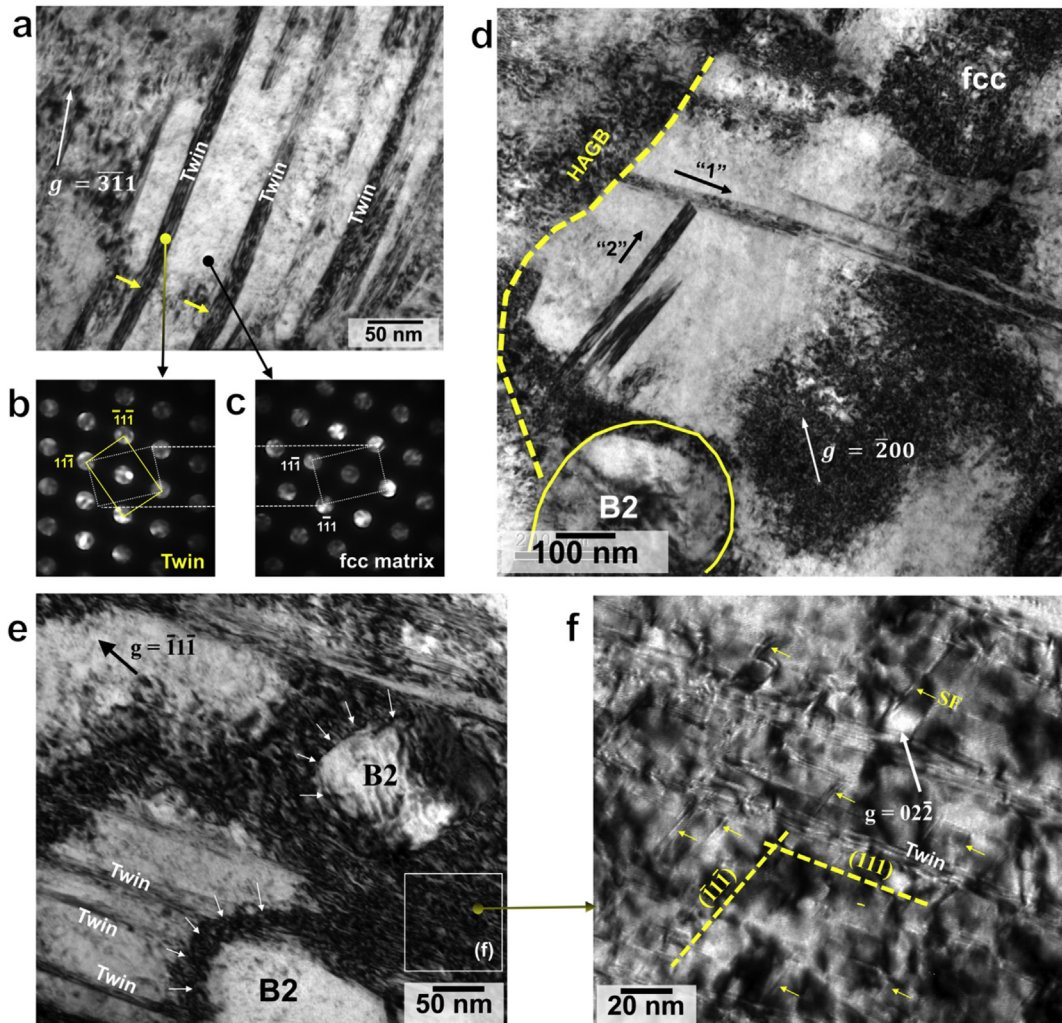


**Fig. 7.** TEM results showing different deformation features inside the fcc grains of fcc-B2 grain clusters in the triplex microstructure. (a) BFTEM recorded with  $\mathbf{g} = \bar{3}\bar{1}1$  shows multiple plates of deformation twins in darker contrast. Other twins are out of contrast under the chosen two-beam condition. (b) and (c) are respectively  $[011]_{\text{fcc}}$  microdiffraction patterns from one of the twins and parent fcc matrix. The micro-diffraction patterns were recorded by orienting the foil approximately along  $[011]_{\text{fcc}}$ . The solid and dotted rectangular motifs show the 2-fold symmetry in the twin and fcc matrix, respectively. (d) BFTEM recorded with  $\mathbf{g} = 200$  depicts the probable origin of the deformation twins from B2-fcc triple junction and a high angle grain boundary (HAGB). The imaging condition also revealed dense dislocations (for example, see the lower left-hand corner). These results indicate substantial twinning in triplex microstructure compared to the single-phase fcc microstructure. BFTEM of deformation microstructure near the B2 precipitates reveal the presence of – (e) twins within fcc and dislocation contrast inside B2, and (f) stacking faults and twins within fcc. Note that the image in (f) was recoded from a region close to the B2 precipitates shown in (e).

tens of nanometers into the adjoining fcc grain, respectively. Formation of such stacking faults near the fcc-B2 interfaces have been studied earlier [33] and is thought to be a mechanism for accommodating local interfacial stresses (more discussion latter). Crucially, the TEM results reveal that the “hard” intermetallic B2 grains are capable of exhibiting limited plasticity even at room-temperature under quasi-static loading conditions. The  $\sigma$  phase behaves quite differently as evident from the failure cracks within this phase, which can be seen as a hairline fracture in the BFTEM of Fig. 4a (marked with arrow), and cracks in the SEM of a larger region in Fig. 8e. In some cases, de-bonding at the  $\sigma$ /fcc interface was also observed; yet all these cracks remained confined within the  $\sigma$  grains and did not propagate into the bulk of the triplex microstructure, indicating that the crack tips were blunted by the relatively compliant/ductile, adjacent fcc grains. Taken together, these results indicate that local stresses, that exceed fcc and B2 yield stresses, are accommodated by both “confined crack formation” within and around  $\sigma$  grains and plastic deformation of the B2 grains.

Thus, our detailed TEM observations revealed multiple deformation mechanisms in the fcc-B2- $\sigma$  triplex microstructure, and that the specific mechanism was related to the neighborhood of the deforming fcc or B2 grains. These mechanisms corresponded to the two types of neighborhoods observed, i.e., clusters comprising fcc and B2 grains and clusters comprising fcc, B2, and  $\sigma$  grains. The salient features of these mechanisms are described below:

1. Within the fcc-B2 clusters (Region-I of Fig. 2g), coarser deformation twins and dislocation plasticity was the primary deformation mechanism within the fcc grains, and
2. Within the fcc-B2- $\sigma$  clusters (Region-II of Fig. 2g), dislocation plasticity and nano-twinning in the fcc grains, limited dislocation plasticity in the intermetallic B2 grains, and confined crack formation in and around the  $\sigma$  grains, were the primary deformation mechanisms.

While these experimentally observed deformation mechanisms are quite interesting, it is not possible to explain the rationale

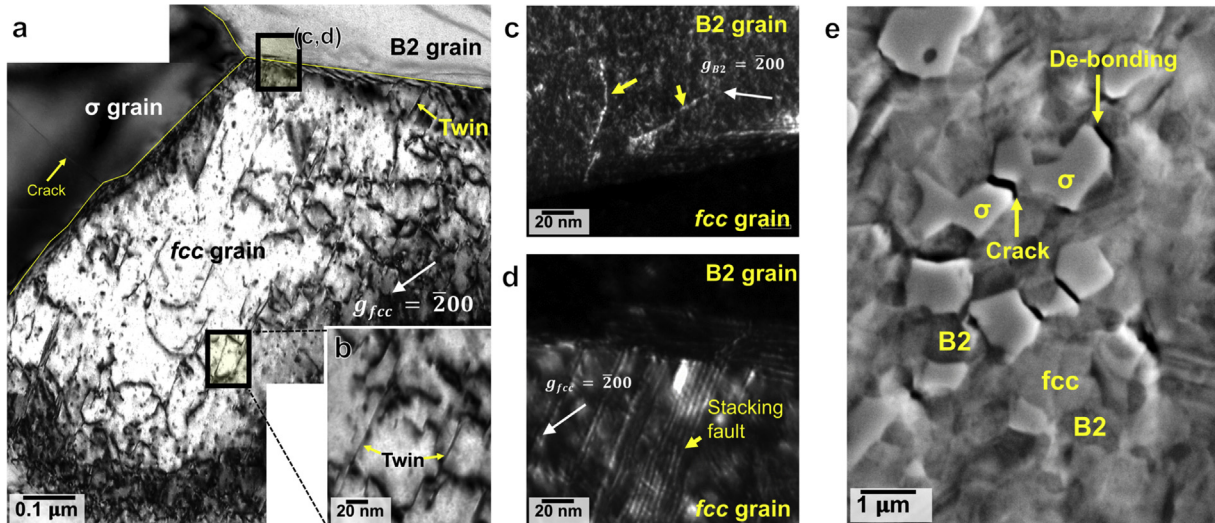


**Fig. 8.** Multiple deformation mechanisms seen inside a fcc grain within fcc-B2- $\sigma$  grain clusters. (a) A composite BFTEM recorded from a fcc-B2- $\sigma$  triple junction with  $g_{fcc} = \bar{2}00$  show dislocation structure inside fcc grain, a hairline crack inside  $\sigma$  and nanoscale twins near the fcc-B2 interface. (b) Nano-twins are also seen inside the fcc matrix away from any of the inter-phase interfaces. The size scale of these twins is comparable to those seen in the single-phase fcc microstructure. (c) weak-beam dark-field of a fcc-B2 interface show deformation features in brighter contrast: (c) dislocations inside B2 and (d) stacking faults extending into the fcc grain, using  $g_{B2} = 200$  and  $g_{fcc} = \bar{2}00$  respectively. A box on the top of (a) demarcates the selected fcc-B2 region. (e) SEM of the deformed microstructure show the distribution of constrained cracks around  $\sigma$  grains, which correlates with hairline crack seen in the BFTEM of (a). Fcc- $\sigma$  debonding was also observed. These features differ greatly from the fcc-B2 grain clusters and reveal inherent the complexity of the triplex deformation behavior.

underlying the formation of coarse deformation twins within the fcc matrix in case of the fcc-B2 clusters, which were an order of magnitude thicker than the deformation twins observed in the single-phase microstructure (compare Figs. 6c and 7a). Therefore, with the objective of developing a better insight into these deformation mechanisms, especially on the role of the intermetallic B2 phase, a complementary computational study has been carried out, using molecular dynamics (MD) simulations on a model multicrystal fcc-B2 ensemble (i.e. Region-I in Fig. 2g).

### 3.5. MD simulations

The methods section details the molecular dynamics simulation methodology used here. Currently, there exist no standard potential within the embedded atom method (EAM) formalism to simulate equiatomic concentrations of Co, Cr, Fe, Ni and Al [40]. Therefore, we have used Ni-Al-Co Purja-Yamakov-Mishin EAM potential [32], which allowed us to model the fcc and B2 phases in the multicrystal ensemble using Ni and NiAl, respectively. It may be pointed out that high stacking fault energy of pure fcc-Ni (125–150 mJ/m<sup>2</sup> [30,41]) suppresses deformation twinning [21]. Therefore, enhancement of twinning (if any) due to the inclusion of a “plastically harder” B2 NiAl grain will also demonstrate the inherent deformation behavior of microstructures comprising of a ductile “twinable” soft phase (i.e. fcc phase in Region-I of Fig. 2g is modelled with pure-Ni) and a harder phase (i.e. B2 phase in Region-I of Fig. 2g modelled with NiAl).

The multicrystal simulation box comprised of five grains shown by the inset in Fig. 9a. We primarily use the following two model simulation systems with  $50 \times 20 \times 10$  nm<sup>3</sup> dimensions to understand how B2 influences the deformation behavior of the surrounding fcc grains: (i) B2 shares a KS OR with one fcc grains, marked region I in Fig. 2g) and called *KS microstructure* and (ii) absence of B2-fcc OR and called *non-KS microstructure*. The multicrystal simulation box was strained along their length (z-axis or) under uniaxial tension at 300K and strain rates of  $10^7$  and  $10^9$  1/s. Figs. 9 and 10 show the stress versus engineering strain and

snapshots at various strains for our prototypical systems deformed at strain rates of  $10^9$  and  $10^7$  1/s, respectively. The results at higher strain-rate of  $10^9$  1/s was also compared with a reference pure-fcc Ni multicrystal agglomerate.

In Figs. 9 and 10 the deformation in three prototypical microstructures were studied: (1) a *KS microstructure* with a B2 grain in the center of the box, which possessed a Kurdjumov-Sachs orientation relationship with one of the neighboring fcc grain marked FCC-G1 (Figs. 9b and 10 b), (2) a system we call *non-KS microstructure* with a B2 grain in the center of the simulation box (Figs. 9c and 10c), and (3) a system with only pure Ni fcc grains present (only Fig. 9d). The crystallographic orientations and the uniaxial deformation direction are also indicated in each panel of Figs. 9 and 10. In the first two prototype systems discussed above, we only changed the orientations of B2 and FCC-G1 but kept the relative orientations of the other fcc grains fixed with respect to the stress axis. Note that grain sizes are identical in all the systems studied here. Common Neighbor Analysis (CNA) algorithm was used to identify crystallographic environment of atoms and color them on the basis of such environment – fcc (green), B2 (blue), and stacking faults and twins (red for hcp coordination) [36]. Atoms at the grain boundaries (GBs) are colored white.

The stress-strain plot shown in Supplementary Fig. 9a depicts the mechanical response of our prototype systems. The onset of yielding appears to occur at ~5 GPa and 3–3.5% strains. However, the location of the first SF, demarcated by the  $1/6<112>$  partial, in the KS system occurs at the fcc-B2 triple junction at 3.2% strain (see Fig. 9b). In the case of non-KS and fcc prototype systems, partials nucleate at the fcc-grain triple junctions at 3.2% and 3.6% strains (see Fig. 9c and d respectively). We emphasize that for 3.2–4.6% strains, the pure fcc system only contained SFs, rather than twins. Above 4.6% strains, the initial SFs transform into twins in both the KS and non-KS systems. At 6.0% strain, additional twins were observed in both KS and non-KS microstructures, where they seem to form at non-KS fcc-B2 interfaces and fcc-fcc GBs. At this stage a twin also formed at the GBs of the fcc microstructure, but the deformation was dominated by  $1/6<110>$  Lomer-Cottrell (LC) locks.

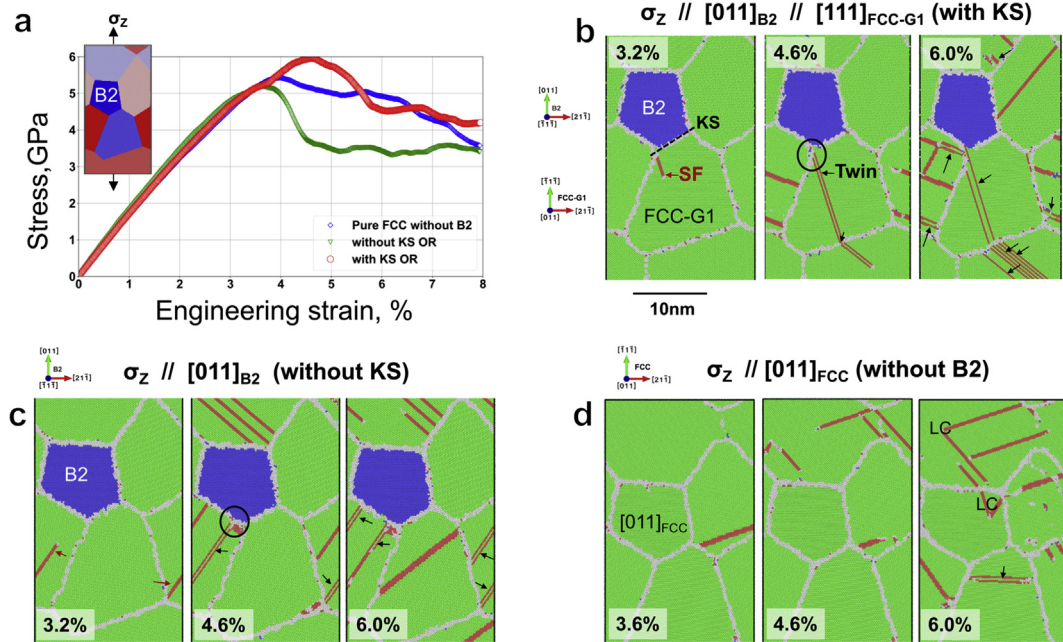


**Fig. 9.** MD simulations performed at  $10^9$  1/s are summarized in this figure. (a) The engineering stress–engineering strain plots of our three prototypical systems are shown here. (b)–(d) illustrate the key atomistic deformation processes in our three prototypical systems wherein B2 shares a KS OR with one fcc grain (panel (b)), no KS OR exists between fcc–B2 (figure (c)), and only fcc grains exist without B2 (panel (d)).

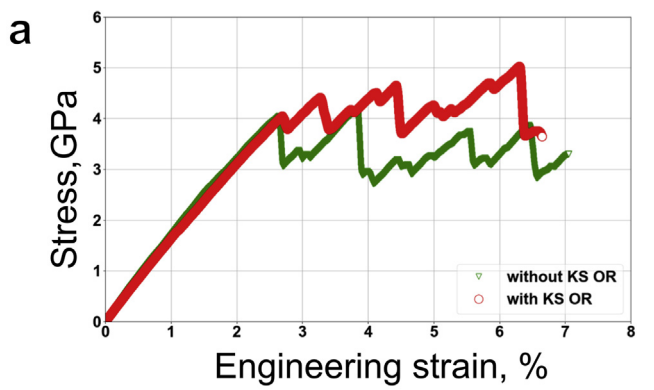


**Fig. 10.** MD simulations performed at  $10^7$  1/s are summarized in this figure. (a) The engineering stress–engineering strain plots of two of our three prototypical systems are compared here. (b)–(c) illustrate the key atomistic deformation processes in these two prototypical systems wherein B2 shares a KS OR with one fcc grain (panel (b)) and no KS OR exists between fcc–B2 (panel (c)). Note that the two systems are compared for deformation at similar strains. Deformation mechanisms observed at a smaller strain rate of  $10^7$  1/s are comparable to  $10^9$  1/s, although there are differences in the details of their respective stress–strain plots. Nonetheless, effect of B2 on twinning is independent of strain rate.

A careful comparison of the deformation in these three microstructures demonstrated that the harder B2 facilitates twinning in fcc matrix. Interestingly, this B2-enhanced twinning appears to be independent of strain rate, because deformation of KS and non-KS also show a similar preponderance of twins (compare Fig. 9b and c and 10b–c). Crucially, the comparison of deformation mechanisms in the fcc–B2 (Fig. 9b and c and 10b–c) and pure fcc (Fig. 9c) revealed the underlying role of harder B2 phase on promoting deformation twins in the neighboring fcc grains, which characteristics are in excellent agreement with the TEM observations (Figs. 7a and 8d).

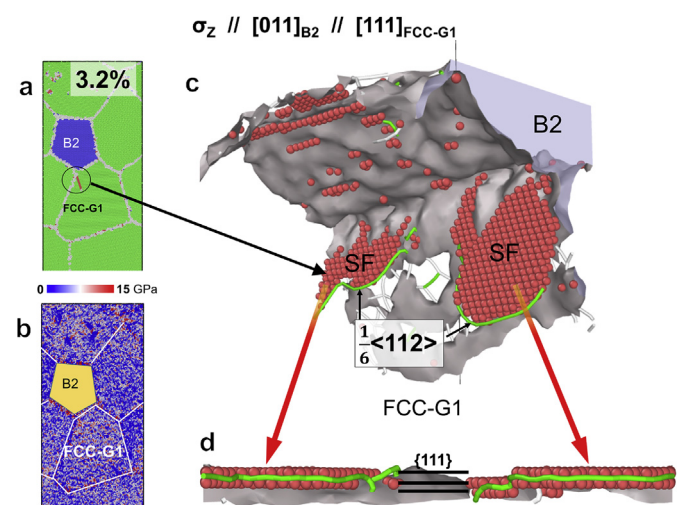


**Fig. 11.** MD simulations showing the early stages of twining via SF formation in simulation box strained at  $10^9$  1/s. (a) SF is seen to emerge from the fcc–B2 triple junction, which contains a KS OR. (b) Shows a higher stress distribution in the KS oriented fcc grain (FCC-G1). (c) and (d) show the two different views of coplanar SFs and 1/6<112> partials in the same grain. Our MD simulations indicated that the presence of B2 enhances twin formation, and this deformation mode is amplified when KS OR is shared between B2 and fcc.

We have further examined the enhancement in twinning seen in the fcc-B2 KS OR simulations (Fig. 9b for  $10^9$  1/s), by probing the dislocation structure and stress distribution at a lower 3.2% strain in Fig. 11a–d. At this early stage of deformation, SFs emanate from the fcc-B2 triple junction (circled in Fig. 11a), because that region had a higher (~5–15 GPa) local stress distribution in the surrounding fcc grain, i.e. FCC-G1 in Fig. 11b. Under quasistatic conditions, the local stresses are expected to be lower, corresponding to UTS value of around 1 GPa. Nonetheless, our simulations indicate that high stresses at the triple junctions will drive the emission of  $1/6<112>$  partials, which are bound to two SFs on the same (111) (Fig. 11c and d). According to the mechanism proposed by Mahajan and colleagues (Fig. 1 in Ref. [20] and Fig. 2 in Ref. [22] respectively), creation of two coplanar SFs is a prerequisite for twin formation. The two partials bounding two such SFs subsequently interact under stress to form a twin nucleus (see snapshot at 4.6% Fig. 9b), which grow by acquiring additional  $1/6<112>$  partials or SFs (i.e. Figs. 9b and 10b).

Finally, we note that in our MD simulations the flow stress of KS microstructure was ~1 GPa higher than the non-KS system for both strain-rates studied here (Figs. 9a and 10a). This difference appears only in the KS OR system because all other factors such as the size and orientations of other fcc grains were held constant in the simulations. As mentioned earlier, the constraint imposed by the KS OR locally increases the stress levels (see Fig. 11) and promotes extensive twining (compare Fig. 9b and c, and Fig. 10b and c), which causes the overall increase in the flow stress of the KS microstructure. Interestingly, our simulations also show that the pure fcc microstructure had a higher flow stress than non-KS microstructure (Fig. 9a). A comparison of deformation features at 6% strain levels of non-KS and fcc microstructures revealed very high density of LC locks in the fcc microstructure, which leads us to conclude that stress levels in the non-KS microstructure (without the constraining effect of KS OR) is not as high. Furthermore, since the LCs are sessile they do not readily emit partials to form twins like the triple junctions and GBs. LCs were difficult to identify in the heavily deformed conditions employed in this study. However, such deformation modes have been reported in partially deformed (~5% strain) Al<sub>0.1</sub>CoCrFeNi HEA using TEM-based observations [12]. Thus, taken together, Figs. 9–11, by using the Ni–Al–Co Purja–Yamakov–Mishin EAM potential, qualitatively captures the deformation behavior of the deformation mechanism seen in these types of fcc-based HEAs.

More importantly, our atomistic simulations of uniaxial tensile deformation of polycrystalline microstructures containing hard-intermetallic and soft-fcc grains provide insight that the generation of high local stresses at fcc-intermetallic triple junctions create precursory partials necessary to nucleate and grow deformation twins.

#### 4. Discussion

Complementary insights gained from MD simulations can help qualitatively explain the complex deformation mechanisms seen in our triplex microstructure's regions-I and II (Figs. 2g, 7 and 8). Local stresses generated at inter-phase boundaries such as triple junctions and bi-phase interfaces, appear to be accommodated by two distinct mechanisms. First, stresses near the fcc-B2 multiphase grain clusters are relieved by the nucleation and growth of deformation twins (Fig. 7d). WBDF contrast seen in Fig. 8d can be viewed as collection of precursory SFs that will trigger the nucleation of twins at the fcc-B2 interfaces. Second, *confined cracking* within  $\sigma$ -grains and *de-bonding* of fcc– $\sigma$  interface can also relieve the local stresses (Fig. 8e). Our simulations suggest that local stresses are sufficiently high to cause limited plasticity within the B2 grains in both regions

(Figs. 7d and 8c), which also likely contribute to the overall ductility of the triplex microstructure. Finally, higher strain hardenability of the triple microstructure can be attributed to multiple factors such as interaction between coarser twins (Fig. 7d), twin-dislocations interactions (Figs. 7a and 8b), interactions between dislocations in regions with high dislocation density (Fig. 7d) and inside a fcc-grain (Fig. 8a). In contrast, only twin-dislocation and dislocation-dislocation interactions are evident in the deformation of single-phase materials (Fig. 6).

Finally, few comments are required regarding the role of stacking fault energies (SFEs) on the deformation behavior of fcc phase in the triplex microstructure. A recent study on the deformation behavior of Al<sub>0.1</sub>CoCrFeNi HEA revealed that this alloy has very low SFE, i.e. 6–21 mJ/m<sup>2</sup> [12]. Another study has also postulated an inverse relationship between Al content and SFE [42]. While SFE of the fcc phase in the triplex microstructure was not measured, these literature reports suggest that the depletion of Al from the fcc, due to B2 formation, will lower the SFE. Thus, in addition to high local stress (exceeding critical stress required for twin nucleation), presumably a contribution from lower SFE promotes favorable conditions for the nucleation and growth of deformation twins.

#### 5. Summary

This work demonstrates that tuning the compositional space of our HEA system yields a novel thermodynamically (meta) stable fcc-B2– $\sigma$  triplex microstructure. This novel microstructure possesses an excellent strength-ductility combination that substantially exceeds commercial titanium alloys and approaches that of many steels. We show that this significant change is due to the presence of a normally hard brittle  $\sigma$  and B2 intermetallic compounds directly promotes deformation twinning and strain hardening behavior of a plastically softer fcc matrix phase. This discovery opens up a new pathway that leverages deformation twinning in high strength precipitation hardened HEAs to achieve excellent strain hardenability and uniform elongation. We believe that such microstructural design of HEAs is paradigm shift from conventionally accepted wisdom that higher strength typically sacrifices strain hardenability and ductility.

#### Acknowledgements

The work was performed under a cooperative agreement between the Army Research Laboratory and the University of North Texas (W911NF-16-2-0189). Microscopy was performed at the Materials Research Facility at UNT. DC and SGS also acknowledges computing resources provided by the high-performance computing facilities at UNT (Talon 3) and Texas Advanced Computing Center (Stampede).

#### Appendix A. Supplementary data

Supplementary data to this article can be found online at <https://doi.org/10.1016/j.actamat.2018.12.010>.

#### References

- [1] H. Mecking, U.F. Kocks, Kinetics of flow and strain-hardening, *Acta Metall.* 29 (11) (1981) 1865–1875.
- [2] G.E. Dieter, *Mechanical Metallurgy*, vol. 3, McGraw-Hill, New York, 1986.
- [3] John Wyrill Christian, Subhash Mahajan, Deformation twinning, *Prog. Mater. Sci.* 39 (1–2) (1995) 1–157.
- [4] De Cooman, C. Bruno, Yuri Estrin, Sung Kyu Kim, Twinning-induced plasticity (TWIP) steels, *Acta Mater.* 142 (2018) 283–362.
- [5] O. Bouaziz, N. Guelton, Modelling of TWIP effect on work-hardening, *Mater. Sci. Eng., A* 319 (2001) 246–249.

- [6] I. Gutierrez-Urrutia, D. Raabe, Dislocation and twin substructure evolution during strain hardening of an Fe-22 wt.% Mn-0.6 wt.% C TWIP steel observed by electron channeling contrast imaging, *Acta Mater.* 59 (16) (2011) 6449–6462.
- [7] Bo Qin, *Crystallography of TWIP Steel*, Pohang University of Science and Technology, 2007.
- [8] Yong Zhang, et al., Microstructures and properties of high-entropy alloys, *Prog. Mater. Sci.* 61 (2014) 1–93.
- [9] D.B. Miracle, O.N. Senkov, A critical review of high entropy alloys and related concepts, *Acta Mater.* 122 (2017) 448–511.
- [10] T. Borkar, et al., A combinatorial assessment of Al<sub>x</sub>CrCuFeNi<sub>2</sub> (0 < x < 1.5) complex concentrated alloys: microstructure, microhardness, and magnetic properties, *Acta Mater.* 116 (2016) 63–76.
- [11] A.J. Zaddach, et al., Mechanical properties and stacking fault energies of NiFeCrCoMn high-entropy alloy, *JOM (J. Occup. Med.)* 65 (12) (2013) 1780–1789.
- [12] X.D. Xu, et al., Transmission electron microscopy characterization of dislocation structure in a face-centered cubic high-entropy alloy Al0.1CoCrFeNi, *Acta Mater.* 144 (2018) 107–115.
- [13] Zi Jiao Zhang, et al., Nanoscale origins of the damage tolerance of the high-entropy alloy CrMnFeCoNi, *Nat. Commun.* 6 (2015) 10143.
- [14] Frederik Otto, et al., The influences of temperature and microstructure on the tensile properties of a CoCrFeMnNi high-entropy alloy, *Acta Mater.* 61 (15) (2013) 5743–5755.
- [15] M. Komarasamy, et al., Effect of microstructure on the deformation mechanism of friction stir-processed Al0.1CoCrFeNi high entropy alloy, *Materials Research Letters* 3 (1) (2015) 30–34.
- [16] D. Choudhuri, et al., Investigation of plastic deformation modes in Al0.1CoCrFeNi high entropy alloy, *Mater. Chem. Phys.* (2018). <https://doi.org/10.1016/j.matchemphys.2018.05.050>.
- [17] B. Schuh, et al., Mechanical properties, microstructure and thermal stability of a nanocrystalline CoCrFeMnNi high-entropy alloy after severe plastic deformation, *Acta Mater.* 96 (2015) 258–268.
- [18] N. Kumar, et al., High strain-rate compressive deformation behavior of the Al0.1CrFeCoNi high entropy alloy, *Mater. Des.* 86 (2015) 598–602.
- [19] Deep Choudhuri, et al., Crystallographically degenerate B2 precipitation in a plastically deformed fcc-based complex concentrated alloy, *Materials Research Letters* 6 (3) (2018) 171–177.
- [20] S. Mahajan, G.Y. Chin, Formation of deformation twins in fcc crystals, *Acta Metall.* 21 (10) (1973) 1353–1363.
- [21] M.A. Meyers, O. Vohringer, V.A. Lubarda, The onset of twinning in metals: a constitutive description, *Acta materialia* 49 (19) (2001) 4025–4039.
- [22] S. Mahajan, Critique of mechanisms of formation of deformation, annealing and growth twins: face-centered cubic metals and alloys, *Scripta Mater.* 68 (2) (2013) 95–99.
- [23] Rodney J. McCabe, et al., The critical role of grain orientation and applied stress in nanoscale twinning, *Nat. Commun.* 5 (2014) 3806.
- [24] The Determination of the Elastic Field of an Ellipsoidal Inclusion, and Related Problems.
- [25] Toshio Mura, *Micromechanics of Defects in Solids*, Springer Science & Business Media, 2013.
- [26] Bharat Gwalani, et al., Modifying transformation pathways in high entropy alloys or complex concentrated alloys via thermo-mechanical processing, *Acta Mater.* 153 (2018) 169–185.
- [27] Influence of Fine-scale Alpha Precipitation on the Mechanical Properties of the Beta Titanium Alloy Beta-21S.
- [28] N. Kumar, et al., Strength and ductility optimization of Mg-Y-Nd-Zr alloy by microstructural design, *Int. J. Plast.* 68 (2015) 77–97.
- [29] Steve Plimpton, Fast parallel algorithms for short-range molecular dynamics, *J. Comput. Phys.* 117 (1) (1995) 1–19.
- [30] GP Purja Pun, V. Yamakov, Y. Mishin, Interatomic potential for the ternary Ni-Al-Co system and application to atomistic modeling of the B2-L10 martensitic transformation, *Model. Simulat. Mater. Sci. Eng.* 23 (6) (2015) 065006.
- [31] S. Karelw, et al., Effect of Li on the deformation mechanisms of nanocrystalline hexagonal close packed magnesium, *Comput. Mater. Sci.* 126 (2017) 252–264.
- [32] Pierre Hirel, Atomsk: a tool for manipulating and converting atomic data files, *Comput. Phys. Commun.* 197 (2015) 212–219.
- [33] D. Choudhuri, R. Banerjee, S.G. Srinivasan, Uniaxial deformation of face-centered-cubic (Ni)-ordered B2 (NiAl) bicrystals: atomistic mechanisms near a Kurdjumov-Sachs interface, *J. Mater. Sci.* 53 (8) (2018) 5684–5695.
- [34] Dennis C. Rapaport, Dennis C. Rapaport Rapaport, *The Art of Molecular Dynamics Simulation*, Cambridge university press, 2004.
- [35] D. Choudhuri, R. Banerjee, S.G. Srinivasan, Uniaxial deformation of face-centered-cubic (Ni)-ordered B2 (NiAl) bicrystals: atomistic mechanisms near a Kurdjumov-Sachs interface, *J. Mater. Sci.* 53 (8) (2018) 5684–5695.
- [36] Alexander Stukowski, Karsten Albe, Extracting dislocations and non-dislocation crystal defects from atomistic simulation data, *Model. Simulat. Mater. Sci. Eng.* 18 (8) (2010) 085001.
- [37] Zepeda-Ruiz, A. Luis, et al., Probing the limits of metal plasticity with molecular dynamics simulations, *Nature* 550 (7677) (2017) 492.
- [38] N. Kumar, et al., Friction stir processing of a high entropy alloy Al 0.1 CoCrFeNi, *JOM (J. Occup. Med.)* 67 (5) (2015) 1007–1013.
- [39] El-Danaf Ehab, Surya R. Kalidindi, Roger D. Doherty, Influence of grain size and stacking-fault energy on deformation twinning in fcc metals, *Metall. Mater. Trans.* 30 (5) (1999) 1223–1233.
- [40] Siros Asgari, et al., Strain hardening regimes and microstructural evolution during large strain compression of low stacking fault energy fcc alloys that form deformation twins, *Metall. Mater. Trans.* 28 (9) (1997) 1781–1795.
- [41] NIST interatomic potentials repository project, Available at: <https://www.ctcms.nist.gov/potentials/>.
- [42] S.G. Ma, et al., A successful synthesis of the CoCrFeNiAl0.3 single-crystal, high-entropy alloy by Bridgman solidification, *JOM (J. Occup. Med.)* 65 (12) (2013) 1751–1758.